Thermal Convection, Magnetic Field, and Differential Rotation in Solar-type Stars

(太陽型星における熱対流、磁場、そして差動回転)

平成25年12月 博士(理学)申請

東京大学大学院理学系研究科
地球惑星科学専攻
堀田　英之

Doctoral thesis

Thermal Convection, Magnetic Field, and Differential Rotation in Solar-type Stars

Hideyuki Hotta

Department of Earth and Planetary Science
School of Science, The University of Tokyo

December 2013

Abstract

Turbulent thermal convection fills the solar convection zone. Understanding thermal convection is crucial for the transport of energy and angular momentum, and the generation and the transport of magnetic field. The central interest in this thesis is the interaction of small- and large-scale convection in the solar and stellar convection zone. To this end, we develop a significantly efficient numerical code that is able to cover broad temporal and spatial scales. We adopt the reduced speed of sound technique (RSST). The RSST is simple to implement and requires only local communication in parallel computations. In addition, this method allows performing simulations without neglecting important physical processes including the solar near surface and achieves small-scale convection in the global domain.

Using the numerical code, we perform non-rotating high-resolution calculations of solar global convection, which resolve convective scales of less than 10 Mm. The main conclusions of this study are the following. 1. The small-scale downflows generated in the near surface layer penetrate down to deeper layers and excite small-scale turbulence in the region of $> 0.9R_\odot$, where $R_\odot$ is the solar radius. 2. In the deeper convection zone ($< 0.9R_\odot$), the convection is not affected by the location of the upper boundary. 3. Using an LES (Large Eddy Simulation) approach we achieved small-scale dynamo action and maintained a field of $0.15 - 0.25B_{\rm eq}$ throughout the convection zone, where $B_{\rm eq}$ is the equipartition magnetic field to the kinetic energy. 4. The overall dynamo efficiency significantly varies in the convection zone as a consequence of the downward directed Poynting flux and the depth variation in the intrinsic convective scales. For a fixed numerical resolution the dynamo relevant scales are better resolved in the deeper convection zone and are therefore less

1

affected by numerical diffusivity, i.e. the effective Reynolds numbers are larger.

Then, we carry out high-resolution calculation of thermal convection in the spherical shell with rotation to reproduce the near surface shear layer (NSSL). It is thought that the NSSL is maintained by thermal convection for small spatial scales and short time scales, which causes a weak rotational influence. The calculation with the RSST succeeds in including such a small scale as well as large-scale convection and the NSSL is reproduced especially at high latitude. The maintenance mechanisms are the following. The Reynolds stress under the weak influence of the rotation transports the angular momentum radially inward. Regarding the dynamical balance on the meridional plane, in the high latitude positive correlation $\langle v_r' v_\theta' \rangle$ is generated by the poleward meridional flow whose amplitude increases with the radius in the NSSL and negative correlation $\langle v_r' v_\theta' \rangle$ is generated by the Coriolis force in the deep convection zone. The force caused by the Reynolds stress compensates the Coriolis force in the NSSL.

Acknowledgments

Contents

Part I
General Introduction

This part serves as the introduction. Fig. 1.1 is a schematic of the overview of the solar interior. In the sun, a static radiative zone and turbulent convection zone exist. The convection zone is filled with turbulent thermal convection that transports the energy and angular momentum. On account of the significant change in the pressure scale height from the base of the convection zone (60,000 km) to the photosphere (300 km), the convection size drastically changes along the radius. This change is the central issue of this thesis. The energy transport is one of the most important factors in solar stratification models (§1.1). The angular momentum transport generates mean flows, such as differential rotation and meridional flow (§1.2). The drastic change in the time scale of the convection causes the shear layer near the surface. In the introduction, we discuss the current understanding on the basis of the previous studies and the remaining problems. The goals of this thesis are discussed in §5.
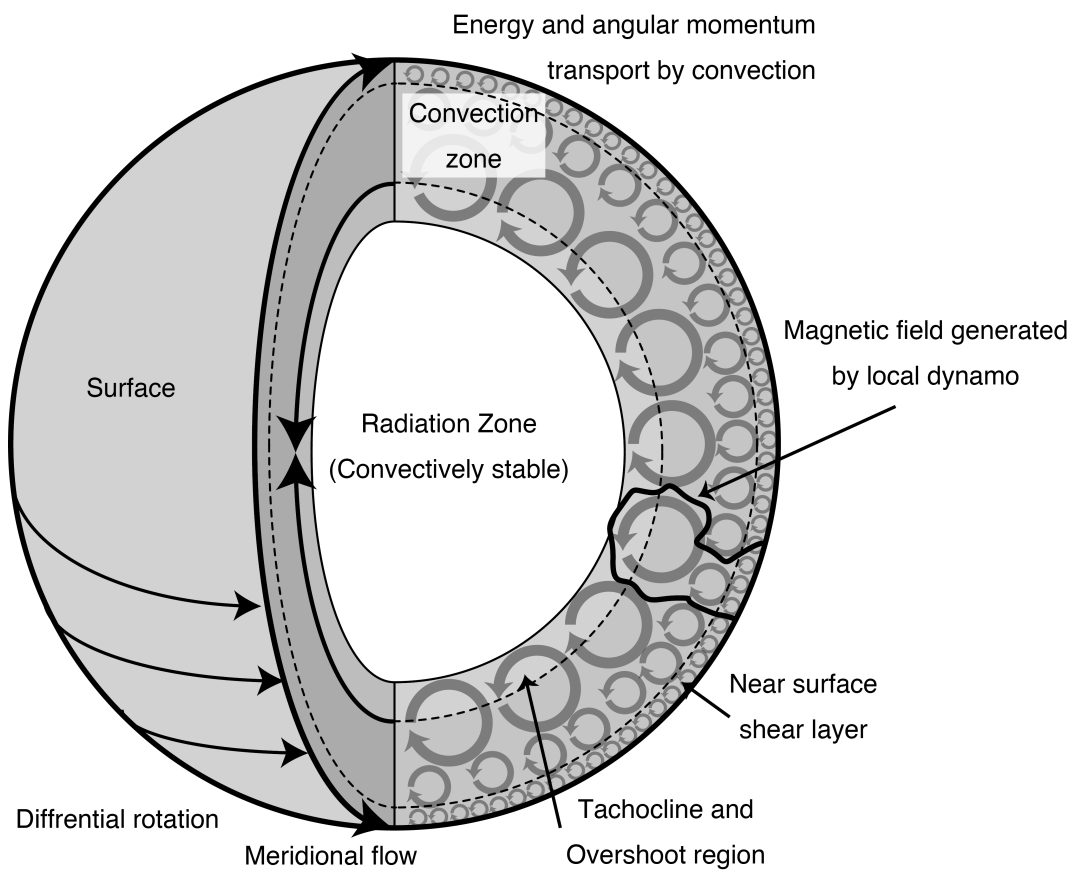
Figure 1.1: The overview of the solar interior.

1   Solar Structure and Mean Flow

1.1   Solar Structure

The sun consists of the radiative zone (from the center to $0.715R_\odot$) and the convection zone (from $0.71R_\odot$ to the surface), where $R_\odot$ is the solar radius($=$ 6.960×10^{10} cm). Fig. 1.2 shows the distribution of physical variables, i.e., gravitational acceleration, density etc., which are taken from the solar standard model (Model S: Christensen-Dalsgaard et al., 1996). Solar luminosity can be estimated from observations ($L_\odot = 3.84 \times 10^{33}$ erg s^{-1}). The other variables in the solar interior are calculated by using the observed luminosity and surface abundance under the assumptions of (1) spherical symmetricity (one dimension), (2) hydrostatic equilibrium, i.e., the balance of the pressure gradient and the gravity force, and (3) thermal equilibrium, i.e., the energy balance between nuclear fusion and transport. The effects of rotation and magnetic field are not included in the solar standard model. Because the plasma temperature exceeds 10^7 K near the core, energy is continuously generated by nuclear fusion. In the radiative zone, this energy is transported by efficient radiation. From $0.2R_\odot$ to $0.715R_\odot$ (the base of the convection zone), the radiative diffusion transports all solar luminosity, i.e., $L_\odot$ (see Fig. 1.2h). This region is convectively stable. In the convection zone, the radiation is no longer efficient and the atmosphere becomes superadiabatically stratified, i.e., $ds/dr < 0$, where s is the specific entropy. Thus, this zone is characterized by turbulent thermal convection and the convective energy flux dominates over the radiative energy flux.

The convective energy flux, which is required to determine the temperature gradient and accordingly the solar structure, is estimated with the mixing length model

(e.g. Stix, 2004). In this model, the mixing length (l_{mix}), which is the mean free path for each convective parcel, is specified with a constant parameter α_{mix} as: $l_{\mathrm{mix}} = \alpha_{\mathrm{mix}} H_{\mathrm{p}}$, where H_{p} is the pressure scale height. It is assumed that each convective parcel is accelerated by buoyancy along the mixing length. Then a certain type of averaged vertical velocity and its convective energy flux can be estimated with the equation of motion. Once the convective energy flux is estimated one can solve equations to obtain the distribution of entropy and the mixing length parameter simultaneously (α_{mix}).

インターネット公表に関する同意が
得られなかったため非公表

Figure 1.2: Various physical quantities in the solar interior from the center to the surface estimated with the solar standard model: (a) gravitational acceleration (b) absolute value of the specific entropy gradient (c) density (d) gas pressure (e) pressure scale height (f) temperature (g) radiative diffusivity (h) radiative luminosity. The values are obtained from Christensen-Dalsgaard et al. (1996) and his website.

The results of the solar standard model are confirmed with global helioseismol-

ogy data. The solar global oscillation observed at the photosphere is described with spherical harmonics (Y_{lm}) in horizontal space and Fourier transforms in time. The harmonic components are compared with the oscillations that are computed with the solar model after assuming linear and adiabatic perturbations. When the residuals of the model with respect to observations are assumed linear, inversion can be performed to obtain information on the solar interior (see also Stix, 2004). Although there is an unexplained anomaly at the base of the convection zone, the residuals between the solar standard model and helioseismology are small. $\delta c_{\rm s}^2 / c_{\rm s}^2$ is typically 10^{-3} where $c_{\rm s}^2$ is the square of the speed of sound and $\delta c_{\rm s}^2$ is its difference (Basu et al., 1997).

1.2 Observation of Solar Mean Flow, Differential Rotation and Meridional Flow

Helioseismology has also revealed the mean structure of the solar flow such as differential rotation (global helioseismology) and meridional flow (local helioseismology).

The solar differential rotation on the surface was first observed by Christoph Scheiner as early as 1630 by using the motion of the sunspots. Then, in 1855 Carrington started the first quantitative observation of the solar rotation (see review by Beck, 2000). Although several researchers expected the existence of a shear layer below the surface with different rotation rate between sunspots and Doppler velocity (see the introduction in part IV), the internal structure of the solar differential rotation remained unknown until the advent of helioseismology. Solar rotation is fast enough to break the spherical symmetry of global oscillation and causes frequency splitting in terms of the azimuthal order m owing to the asymmetry in travel times

between the eastward and westward waves (see review by Christensen-Dalsgaard, 2002). Fig. 1.3 shows the obtained result of the internal differential rotation (originally from Schou et al., 1998).

インターネット公表に関する同意が
得られなかったため非公表

Figure 1.3: The distribution of angular velocity in the solar interior (after Thompson et al., 2003); the distribution (a) in the meridional plane and (b) at selected latitudes. These are obtained by using the MDI/SOHO (see also Miesch, 2005).

The result shows five important features regarding the internal rotation. First the equator region rotates faster than the polar region. Note that the reliability of the data diminishes around the polar region. Second the distribution of the angular velocity is not cylindrical but conical in contrast to the Taylor-Proudman theory (see the theoretical discussion in §2). Third the radiation zone rotates almost rigidly at intermediate rate between the equator and the pole. Forth, there is a thin shear layer between the convection zone and radiation zone called tachocline. Although the

details of the structure are controversial, the tachocline is thought to be ellipsoidal. For example, Charbonneau et al. (1999) show that the center of the tachocline is $r_t/R_\odot = 0.693 \pm 0.003$ at the equator which is below the base of the convection zone and $r_t/R_\odot = 0.717 \pm 0.003$ at the pole which is slightly above the base. Although the thickness of the tachocline is still controversial, Charbonneau et al. (1999) show that the thickness is from $\Delta_t = 0.016 R_\odot$ at the equator to $\Delta_t = 0.038 R_\odot$ at the pole. The fifth important feature is the near surface shear layer (NSSL). There are significant deviations from the Taylor-Proudman state above $r = 0.95 R_\odot$. In this layer, the angular velocity increases along the radius (see also the introduction of Part IV). The detailed distribution of the NSSL is studied by Corbard & Thompson (2002), using f modes from MDI data. They measured the gradient of the NSSL as about -400 nHz$/R_\odot$. The rotation rate was found to vary almost linearly with depth Howe (2009). We note that the deviation from the Taylor-Proudman state in the NSSL is larger than that in the deep convection zone. This shear layer is the one of the targets of this thesis.

The meridional flow, known as the mean flow on the meridional plane, i.e., $\langle v_r \rangle$ and $\langle v_\theta \rangle$, is also observed on the surface with Doppler measurements (Hathaway et al., 1996; Hathaway, 1996), where the parenthesis $\langle \rangle$ denotes the zonal average. These observations show the poleward meridional flow with the amplitude of a several 10 m s^{-1} (Giles et al., 1997). Using the global helioseismology, i.e., global-standing mode of the acoustic wave, it is difficult to distinguish the effect of the meridional flow as a perturbation of the standing-mode from those of magnetic field and the centrifugal force since the amplitude of the meridional flow is relatively small (~ 10 m s^{-1}) compared to the convection at the surface (~ 1 km s^{-1}) and the speed

of rotation (2 km s^{-1}). Duvall et al. (1993) suggested a new technique to investigate the flow structure in the solar interior; they called it "local helioseismology." In the time-distance method of local helioseismology, a correlation between two specific points is estimated. The travel time difference between the forward and backward waves is sensitive to the internal structure of the horizontal flow. The Gile et al.'s (1997) results are shown in the Fig. 1.4. Although the result show only a fraction

インターネット公表に関する同意が
得られなかったため非公表

Figure 1.4: Figure is from Giles et al. (1997) and shows the average travel time difference. The solid line is the best fit using the function $\delta\tau = a_1 \cos\lambda + a_2 \cos 2\lambda$. Using this model, the travel time can be interpreted as the mean flow. In this model, the 12.1 m s^{-1} flow corresponds to 1 s travel time1 difference. The positive velocity corresponds to northward movement.

of the meridional flow in the solar convection zone (the upper 4% in radius and ±60 degree in latitude), there is a poleward meridional flow in both hemispheres. Haber et al. (2002) also showed the asymmetry of the meridional flow about the equator and its dependence on time. In a certain phase of the solar cycle there is counter flow in the polar region (Fig. 1.5)

Recent observation by Zhao et al. (2013) shows a 2D distribution of the meridional flow (Fig. 1.6a). Although the reliability in deeper layer is controversial, a

インターネット公表に関する同意が
得られなかったため非公表

Figure 1.5: The figure is from Haber et al. (2002). The structure of the meridional flow is averaged in time and longitude. The time interval in these figures is six years. The gray-shaded area shows the region with southward flow (poleward at south hemisphere).

インターネット公表に関する同意が
得られなかったため非公表

Figure 1.6: The figure is from Zhao et al. (2013) with modifications. Meridional flow profile, obtained with the acoustic travel time. Panel (a) shows a flow profile on the meridional plane, with positive velocity directing northward. Panel (b) shows a flow profile as a function of latitude averaged over $0.90 - 0.93R_\odot$ (red line) and $0.95 - 0.98R_\odot$ (black line).

return (equatorward) flow is seen in the middle of the convection zone and another cell exists in the lower part of the convection zone, i.e., multi-cell structure. In the near surface layer, the coherent poleward flow is observed, which is consistent with previous studies. Fig. 1.6b indicates that the amplitude of the meridional flow increases along the radius. This result is important for understanding of the NSSL in Part IV.

2 Theory and Numerical Calculation for Differential Rotation and Meridional Flow

2.1 Gyroscopic Pumping and Thermal Wind Balance

To understand the maintenance mechanism of the mean flow, i.e., the differential rotation and meridional flow, the gyroscopic pumping and thermal wind balance equations, which we discuss in this section, are helpful (Rempel, 2005; Miesch, 2005; Miesch & Hindman, 2011).

In the beginning, the Reynolds stress is reviewed. First, we consider the equation of motion in fluid dynamics:

$$\rho_0 \frac{\partial \mathbf{v}}{\partial t} = -\nabla \cdot (\rho_0 \mathbf{v}\mathbf{v}) - \nabla p, \tag{1.1}$$

where ρ_0, $\mathbf{v}$, and p is time-independent density, fluid velocity and gas pressure, respectively. Using a kind of ensemble average $\langle \rangle$, which is likely the zonal average at following discussion, the quantities (Q) are divided into the mean part $\langle Q \rangle$ and the perturbed part Q', i.e., $Q = \langle Q \rangle + Q'$. Then, the equation for the mean velocity $\langle \mathbf{v} \rangle$ is expressed as

$$\rho_0 \frac{\partial \langle \mathbf{v} \rangle}{\partial t} = -\nabla \cdot (\rho_0 \langle \mathbf{v} \rangle \langle \mathbf{v} \rangle) - \nabla \cdot (\rho_0 \langle \mathbf{v}' \mathbf{v}' \rangle) - \nabla \langle p \rangle, \tag{1.2}$$

10

where $\langle v' \rangle = 0$ is used. The terms $-\nabla \cdot (\rho_0 \langle \mathbf{v} \rangle \langle \mathbf{v} \rangle)$ and $-\nabla \langle p \rangle$ represent the processes from the mean quantities to the mean quantities. The term $-\nabla \cdot (\rho_0 \langle \mathbf{v}'\mathbf{v}' \rangle)$ represents the effect from the perturbed part to the mean part via the nonlinear coupling of the fluid velocity. The quantity $\rho_0 \langle \mathbf{v}'\mathbf{v}' \rangle$ is called the Reynolds stress. In anisotropic turbulence, nondiagonal terms in the Reynolds stress exist, which cause anisotropic momentum transport.

To derive the equations for gyroscopic pumping and thermal wind balance, we consider the equation of motion without the kinetic viscosity and the magnetic field contributions.

$$\rho_0 \frac{\partial \mathbf{u}}{\partial t} = -\nabla \cdot (\rho_0 \mathbf{u}\mathbf{u}) - \nabla p_1 - \rho_1 g \mathbf{e}_r, \tag{1.3}$$

where p_1, ρ_1, g, and $\mathbf{e}_r$ are the perturbed gas pressure, the perturbed density, the gravitational acceleration, and the unit vector along the radial direction. In the following discussion $\mathbf{u}$ and $\mathbf{v}$ are the fluid velocities at the inertial reference system and the rotating system, i.e., $\mathbf{u} = \mathbf{v} + r \sin\theta \Omega_0 \mathbf{e}_\phi$, where Ω_0 is the rotation rate of the system. The background stratification, ρ_0 and p_0, is assumed to be in spherically symmetric hydrostatic equilibrium, i.e.,

$$0 = -\frac{dp_0}{dr} - \rho_0 g. \tag{1.4}$$

Gyroscopic pumping is derived from the conservation equation for the angular momentum, i.e., originally from the zonal component of the equation of motion

$$
\begin{aligned}
\rho_0 \frac{\partial u_\phi}{\partial t} = {} & -\frac{1}{r^2} \frac{\partial}{\partial r} \left(r^2 \rho_0 u_r u_\phi \right) - \frac{1}{r \sin\theta} \frac{\partial}{\partial \theta} \left(\sin\theta \rho_0 u_\theta u_\phi \right) \\
& -\frac{1}{r \sin\theta} \frac{\partial}{\partial \phi} (\rho_0 u_\phi u_\phi) - \frac{\rho_0 u_\phi u_r}{r} - \frac{\cot\theta \rho_0 u_\phi u_\theta}{r} \\
& -\frac{1}{r \sin\theta} \frac{\partial p_1}{\partial \phi}.
\end{aligned}
\tag{1.5}
$$

11

The zonal component means the ϕ-component in the spherical geometry (r, θ, ϕ), where r and θ are the radius and the colatitude, respectively. Then, we multiply $r \sin \theta$ and define the specific angular momentum as $\mathcal{L} = u_\phi r \sin \theta$. The equation becomes

$$
\begin{aligned}
\rho_0 \frac{\partial \mathcal{L}}{\partial t} &= -\frac{1}{r} \frac{\partial}{\partial r} \left(r^2 \sin \theta \rho_0 u_r u_\phi \right) - \frac{\partial}{\partial \theta} \left(\sin \theta \rho_0 u_\theta u_\phi \right) \\
&\quad - \frac{\partial}{\partial \phi} (\rho_0 u_\phi u_\phi) - \rho_0 u_\phi u_r \sin \theta - \rho_0 u_\phi u_\theta \cos \theta - \frac{\partial p_1}{\partial \phi} \\
&= -\frac{1}{r^2} \frac{\partial}{\partial r} \left[r^2 (r \sin \theta \rho_0 u_r u_\phi) \right] - \frac{1}{r \sin \theta} \frac{\partial}{\partial \theta} \left[\sin \theta (r \sin \theta \rho_0 u_\theta u_\phi) \right] \\
&\quad - \frac{1}{r \sin \theta} \frac{\partial}{\partial \phi} \left[r \sin \theta (\rho_0 u_\phi u_\phi + p_1) \right] \\
&= -\nabla \cdot \left[r \sin \theta (\rho_0 \mathbf{u} u_\phi + p_1 \mathbf{e}_\phi) \right].
\end{aligned} \tag{1.6}
$$

Gyroscopic pumping shows the balance of the angular momentum transport on the meridional plane after the zonal average. When an anelastic approximation is valid for the mean flow $(\nabla \cdot (\rho_0 \langle \mathbf{v}_{\mathrm{m}} \rangle) = 0)$, eq. (1.6) with zonal average is expressed as

$$
\rho_0 \frac{\partial \langle \mathcal{L} \rangle}{\partial t} = -\rho_0 \langle \mathbf{v}_{\mathrm{m}} \rangle \cdot \nabla \langle \mathcal{L} \rangle - \nabla \cdot (r \sin \theta \rho_0 \langle \mathbf{v}_{\mathrm{m}}' v_\phi' \rangle). \tag{1.7}
$$

Then the thermal wind balance equation is derived. The thermal wind balance equation is the originally zonal component of the vorticity equation. For a rotational system with rotation rate Ω_0, the equation of motion, after some algebra, is expressed using the Coriolis force as

$$
\frac{\partial \mathbf{v}}{\partial t} = -(\mathbf{v} \cdot \nabla)\mathbf{v} - \frac{\nabla p_1}{\rho_0} - \frac{\rho_1}{\rho_0} g \mathbf{e}_r + 2\mathbf{v} \times \mathbf{\Omega_0}, \tag{1.8}
$$

where $\mathbf{\Omega_0} = \Omega_0 \mathbf{e_z}$ and $\mathbf{e_z} = \cos \theta \mathbf{e_r} - \sin \theta \mathbf{e}_\theta$ is the unit vector along the rotational axis (z-axis). Using the vector formula

$$
(\mathbf{v} \cdot \nabla)\mathbf{v} = \nabla \left(\frac{v^2}{2} \right) - \mathbf{v} \times (\nabla \times \mathbf{v}), \tag{1.9}
$$

12

and taking the curl of the equation of motion, the vorticity equation is obtained

$$\frac{\partial \omega}{\partial t} = \nabla \times (\mathbf{v} \times \omega) + \nabla \times \left(-\frac{\nabla p_1 + \rho_1 g \mathbf{e_r}}{\rho_0} \right) + \nabla \times (2\mathbf{v} \times \mathbf{\Omega_0}). \qquad (1.10)$$

In the thermal wind equation, the zonal component is focused. Then, the zonal component of the second and third terms in the right-hand side is computed as

$$
\begin{aligned}
\left[\nabla \times \left(-\frac{\nabla p_1 + \rho_1 g \mathbf{e_r}}{\rho_0} \right) \right]_\phi &= \frac{1}{\rho_0^2 r} \frac{d\rho_0}{dr} \frac{\partial p_1}{\partial \theta} + \frac{g}{\rho_0 r} \frac{\partial \rho_1}{\partial \theta} \\
&= -\frac{g}{\rho_0 r} \left[\left(\frac{\partial \rho}{\partial p} \right)_s \frac{\partial p_1}{\partial \theta} - \frac{\partial \rho_1}{\partial \theta} \right] \\
&= \frac{g}{\rho_0 r} \left(\frac{\partial \rho}{\partial s} \right)_p \frac{\partial s_1}{\partial \theta}, \qquad (1.11)
\end{aligned}
$$

and

$$
\begin{aligned}
\left[\nabla \times (2\mathbf{v} \times \mathbf{\Omega}_0) \right]_\phi &= \left[2(\mathbf{\Omega}_0 \cdot \nabla)\mathbf{v_r} - 2(\mathbf{v} \cdot \nabla)\mathbf{\Omega}_0 \right]_\phi \\
&= 2(\mathbf{\Omega_0} \cdot \nabla)v_\phi = 2r \sin\theta \Omega_0 \frac{\partial \Omega_1}{\partial z}, \qquad (1.12)
\end{aligned}
$$

respectively. Subsequently, the zonal average for the vorticity equation is

$$\frac{\partial \langle \omega_\phi \rangle}{\partial t} = [\langle \nabla \times (\mathbf{v} \times \omega) \rangle]_\phi + 2r \sin\theta \Omega_0 \frac{\partial \langle \Omega_1 \rangle}{\partial z} + \frac{g}{\rho_0 r} \left(\frac{\partial \rho}{\partial s} \right)_p \frac{\partial \langle s_1 \rangle}{\partial \theta}. \qquad (1.13)$$

The equations for the mean flows are thus derived. The equations are originally derived from the equation of motion, thus the gyroscopic pumping and the thermal wind balance equation show the time evolution of the angular momentum and the meridional flow, respectively. In the steady state ($\partial/\partial t = 0$), however, the gyroscopic pumping and the thermal wind balance equations determine the meridional flow and the differential rotation, respectively. In the steady state, gyroscopic pumping is

$$\rho_0 \langle \mathbf{v_m} \rangle \cdot \nabla \langle \mathcal{L} \rangle = -\nabla \cdot (r \sin\theta \rho_0 \langle \mathbf{v'_m} v'_\phi \rangle). \qquad (1.14)$$

13

This equation indicates that when the Reynolds stress is given, the meridional flow $\langle \mathbf{v}_\mathrm{m} \rangle$ can be determined. The thermal wind balance equation in the steady state is expressed as

$$-2r\sin\theta\,\Omega_0\frac{\partial\langle\Omega_1\rangle}{\partial z} = [\langle\nabla\times(\mathbf{v}\times\omega)\rangle]_\phi + \frac{g}{\rho_0 r}\left(\frac{\partial\rho}{\partial s}\right)_p\frac{\partial\langle s_1\rangle}{\partial\theta}. \qquad (1.15)$$

This also indicates that when the advection/stretching term ($[\langle\nabla\times(\mathbf{v}\times\omega)\rangle]_\phi$) and the latitudinal entropy gradient are given, the differential rotation $\langle\Omega_1\rangle$ is determined. Note that there is a possibility that the mean flows, $\langle\mathbf{v}_\mathrm{m}\rangle$ and $\langle\Omega_1\rangle$, affect the Reynolds stress in return.

The distribution of the Reynolds stress is required in the direct numerical calculations, otherwise models have to be used (Kitchatinov & Rüdiger, 1995; Küker & Stix, 2001; Rempel, 2005; Hotta & Yokoyama, 2011). The investigations that use direct numerical calculations are reviewed in the next section.

2.2 Numerical Calculations for Differential Rotation and Meridional Flow

There have been numerous studies about differential rotation using the mean-field model in which the thermal convection is treated as the parameterized effect (e.g. Kitchatinov & Rüdiger, 1995; Küker & Stix, 2001; Rempel, 2005; Hotta & Yokoyama, 2011) and the three-dimensional model in spherical shell including thermal convection using the anelastic approximation (Gilman & Miller, 1981; Glatzmaier, 1984; Miesch et al., 2000; Brun & Toomre, 2002; Miesch et al., 2006, 2008; Brun et al., 2011). In this type of numerical calculations, the solar parameters in the standard model are adopted as the background stratification.

The latest conclusions from these studies are summarized as follows: 1. A banana

cell-like convective structure causes the equatorward angular momentum transport (Miesch et al., 2000). 2. Radially inward angular momentum transport is established in almost the whole of the convection zone (Brun & Toomre, 2002). 3. A latitudinal entropy gradient that corresponds to a temperature difference of ~ 10 K between the pole and the equator is required to reproduce the conical profile (Miesch et al., 2006) and the tachocline (Brun et al., 2011).

The banana cell is especially established outside the tangential cylinder ($\sin\theta > r_{\mathrm{base}}/r$, where r_{base} is the location of the base of the convection zone). Because the Coriolis force is expressed as $2\rho_0 \mathbf{v} \times \mathbf{\Omega_0}$, the fluid parcel rotates around the rotational axis when the disturbance from the boundary is not significant. This is analogous to the Larmor motion of the plasma particle, where the Lorentz force is proportional to $\mathbf{v} \times \mathbf{B}$.

This situation is seen in Fig. 1.7a, which was originally suggested by Busse (1970). A topological explanation for the equatorward angular momentum transport is given in Miesch (2005). In the northern hemisphere, the prograde flow ($v'_\phi > 0$) is bent equatorward ($v'_\theta > 0$) and the retrograde flow ($v'_\phi < 0$) is bent poleward ($v'_\theta < 0$). As a result, the correlation is positive $\langle v'_\theta v'_\phi \rangle > 0$. This implies equatorward angular momentum transport. More generally this is explained with the equation of motion on the perturbed velocity along the λ-direction (v'_λ), where λ is the direction perpendicular to the rotation axis. Note that the unit vector in λ is $\mathbf{e_\lambda} = \sin\theta \mathbf{e_r} + \cos\theta \mathbf{e_\theta}$. The equation of motion is expressed as

$$\frac{\partial v'_\lambda}{\partial t} = [...] + 2 v'_\phi \Omega_0. \tag{1.16}$$

15

インターネット公表に関する同意が
得られなかったため非公表

Figure 1.7: (a) Figure is from Busse (1970). The structure of the velocity is homogeneous along the rotational axis and generates columns parallel to the rotational axis (called the "Busse column" or "Taylor column") in rapidly rotating fluid, (b) Figure is from Miesch et al. (2000) with some modifications. At low latitude, there are banana cells.

This shows that the banana cell is likely to generate positive correlation $\langle v'_\lambda v'_\phi \rangle >$ 0, with outward angular momentum transport. This is the essential mechanism accelerating the equator.

Next we discuss the radial angular momentum transport. When the banana cell is not well established, the correlation between the radial and zonal velocities is generated from the radial component of the equation of motion.

$$\frac{\partial v'_r}{\partial t} = [...] - 2v'_\phi \Omega_0 \sin \theta. \tag{1.17}$$

Thus, a negative correlation $\langle v'_r v'_\phi \rangle < 0$ is generated. This implies downward angular momentum transport in the convection zone. In most of the calculations, the angular momentum flux by the Reynolds stress peaks in amplitude around the middle depth of the convection zone. This indicates that the value $-\nabla \cdot (\rho_0 r \sin \theta \langle v'_r v'_\phi \rangle \mathbf{e_r})$ is negative (positive) at the upper (lower) part of the convection zone. Even when the differential rotation is conical, the distribution of the angular momentum is almost cylindrical, i.e., $\nabla \langle \mathcal{L} \rangle \sim d\langle \mathcal{L} \rangle / d\lambda$, because of the factor of $(r^2 \sin^2 \theta)$. Hence gyroscopic pumping becomes

$$\rho_0 \langle \mathbf{v_m} \rangle \frac{d\langle \mathcal{L} \rangle}{d\lambda} = -\nabla \cdot (\rho_0 r \sin \theta \langle v'_r v'_\phi \rangle \mathbf{e_r}). \tag{1.18}$$

Then poleward (equatorward) meridional flow is established at the upper (lower) part of the convection zone with a positive value of $d\langle \mathcal{L} \rangle / d\lambda$.

The discussion then moves to the thermal wind balance equation (1.15), i.e., the conical profile, the tachocline, and the NSSL. Eq. (1.15) indicates that the contributions from the advection/stretching term and/or the entropy gradient are required to maintain the conical profile, the tachocline, and the NSSL, because they are in the non-Taylor-Proudman state $(\partial \langle \Omega_1 \rangle / \partial z \neq 0)$ in steady state. In the convection

zone, the entropy gradient is considered critical (the role of the advection/stretching term is discussed in Part IV). There are two possible mechanisms to generate the latitudinal entropy gradient. The first is an anisotropic correlation of the velocity and entropy $\langle v'_\theta s'_1 \rangle$. In the convection zone, the flow is likely aligned along the rotational axis and the correlation is negative $\langle v'_r v'_\theta \rangle < 0$. In thermal convection, the radial velocity and entropy fluctuation are well correlated $\langle v'_r s'_1 \rangle > 0$, because the hot (cool) plasma moves upward (downward). As a result, a negative correlation $\langle v'_\theta s'_1 \rangle$ that transports the positive entropy poleward is generated. Miesch et al. (2006) calculated that the temperature difference between the pole and the equator generated by this process is approximately 8 K which is not sufficiently large to explain the solar differential rotation. Thus, Miesch et al. (2006) added a latitudinal entropy gradient as a boundary condition at the base of the convection zone. The second mechanism to generate the latitudinal entropy gradient is the penetrating meridional flow originally suggested by Rempel (2005) in his mean-field model. When the anticlockwise meridional flow is established in the northern hemisphere, the downflow at the pole penetrates the overshoot region and generates positive entropy perturbation. The same phenomenon occurs in the upflow at the equator region and negative entropy perturbation is generated. Brun et al. (2011) simultaneously reproduced these two mechanisms and established the conical profile and tachocline in a self-consistent manner.

Finally in this section, the latest numerical calculations are introduced. Miesch et al. (2008) is a state-of-art study which considered the convection zone only. They achieved the highest resolution and provided the latest understanding of the physics in the convection zone. Their upper boundary is at $r = 0.98 R_\odot$ and the resolution

18

インターネット公表に関する同意が
得られなかったため非公表

Figure 1.8: Radial velocity v_r at selected depths in Miesch et al. (2008). (a) $0.98R_\odot$, (b) $0.92R_\odot$, (c) $0.85R_\odot$, and (d) $0.71R_\odot$.

is $N_r \times N_\theta \times N_\phi = 257 \times 1024 \times 2048$, where N_r, N_θ, and N_ϕ are the number of grid points in the radial, latitudinal, and longitudinal direction, respectively. The horizontal grid spacing is approximately 2.2 Mm at the top boundary. Fig. 1.8 shows the distribution of the radial velocity. The spectral peak of the radial velocity is estimated at $l \sim 80$, which corresponds to the horizontal scale of 55 Mm. On account of the low viscosity due to the high resolution, a relatively proper balance of the angular momentum transport between the meridional flow and the Reynolds stress is established. Fig. 1.9 shows the results for the differential rotation, the meridional flow, and the temperature distribution. Miesch et al. (2008) added the latitudinal temperature gradient as boundary condition and established the solar-like conical profile of the differential rotation. The origin of the counter flows near the boundary was not well discussed; nonetheless the prominent one-cell meridional

インターネット公表に関する同意が
得られなかったため非公表

Figure 1.9: (a) Differential rotation, (b) angular velocity at selected latitudes, (c) meridional flow, and (d) mean temperature perturbation in Miesch et al. (2008).

flow was reproduced in the convection zone.

3 Remaining Problems

As discussed in the previous sections, observations, theory, and the numerical calculations have improved our understanding of the convection zone. There are essentially two remaining problems in the numerical calculation: 1. The difficulty in increasing the resolution. 2. The inaccessibility to the real solar surface. The causes are explained in the next section. In this section, the reason why they are required is explained.

There are several reasons why high resolution is required. Some are related to the magnetic field. Zwaan (1987) reported that the magnetic flux of sunspots is from 10^{20} Mx to 10^{22} Mx. At the base of the convection zone, the magnetic strength

is estimated to be 5×10^4 G to reproduce the tilt angle of the sunspot pair (Weber et al., 2011). Several studies suggest that magnetic field with this strength can be generated by explosion processes (Rempel & Schüssler, 2001; Hotta et al., 2012a). These results indicate that the radius of the magnetic flux tube at the base of the convection zone is 2.5 Mm for the largest sunspot. This is comparable with the grid spacing of the current highest resolution calculation (Miesch et al., 2008). To avoid dissipation by numerical diffusivity, at least 10 grid points are required to resolve the flux tube. In addition, Cheung et al. (2006) suggested that the magnetic Reynolds number, which is determined by the resolution, has a significant impact on the behavior of the flux tube.

There is another requirement for the higher resolution owing to local (small scale) dynamo action. The dynamo, especially the stretching, is most effective in small scales. Although some numerical calculations in the local small box reveals the properties of the local dynamo on the photosphere (Vögler & Schüssler, 2007; Pietarila Graham et al., 2010), the turbulent effect on the generation and the transportation of the magnetic field in the convection is unclear because it requires a huge number of grid points to resolve the inertial scale of the turbulence.

A fundamental and important issue which requires high resolution, is the connection between the photosphere and the convection zone. The convection scale in the photosphere is quite small ($\sim$ 1 Mm); hence, the calculation for both the solar global scale (the sun's circumference is 4400 Mm) and the photosphere's small convection also requires a huge number of grid points. This raises two important questions. 1. How does small-scale convection in the near surface layer influence the structure of large-scale convection? 2. How is the NSSL formed and maintained?

Detailed introduction to the NSSL is given in Part IV. The NSSL is thought to be a layer where the rotational influence drastically changes as the time scale of the convection changes. The requirement to address these problems are the accessibility to the solar surface as well as higher resolution. Anelastic approximation, the currently well-adopted method, however, has difficulties with both of them. A new method is adopted in this thesis.

4 Reduced Speed of Sound Technique

Before the problems with the anelastic approximation are explained, the reason why the anelastic approximation is adopted for the numerical calculations of the solar and stellar convection zone needs to be explained. One of the most significant difficulties arises from the large speed of sound, and the related low Mach-number flows throughout most of the convection zone. At the base of the convection zone, the speed of sound is approximately 200 km s^{-1}, whereas the speed of convection is thought to be 50 m s^{-1} (e.g. Stix, 2004). The time step must therefore be shorter on account of the CFL condition in an explicit fully compressible method even when we are interested in phenomena related to convection. To avoid this situation, the anelastic approximation is frequently adopted in which the mass conservation equation is replaced with $\nabla \cdot (\rho_0 \mathbf{v}) = 0$, where ρ_0 is the reference density and $\mathbf{v}$ is the fluid velocity. In this approximation, the speed of sound is assumed infinite and one needs to solve the elliptic equation for pressure, which filters out the propagation of the sound wave. Because the anelastic approximation is applicable deep in the convection zone and the time step is no longer limited by the high speed of sound, the solar global convection has been investigated with this method in many studies

dealing with the differential rotation, the meridional flow, the global dynamo, and dynamical coupling of the radiative zone (Miesch et al., 2000, 2006, 2008; Brun & Toomre, 2002; Brun et al., 2004, 2011; Browning et al., 2006; Ghizaru et al., 2010) as explained in the previous section.

There are, however, two drawbacks in the anelastic approximation. The first is the breakdown of the approximation near the solar surface. Because the convection velocity increases and the speed of sound decreases in the near surface layer ($> 0.98 R_\odot$), they have similar values and the anelastic approximation cannot be applied. The connection between the near surface layer and the global convection is an ongoing challenge (e.g. Augustson et al., 2011). A global calculation, however, which includes all multiple scales, has not been achieved yet.

The second drawback is the difficulty in increasing the resolution. The pseudo-spectral method based on spherical harmonic expansion is frequently adopted, especially for solving the elliptic equation of pressure. In this method, the nonlinear terms require the transformation of physical variables from real space to spectral space and vice versa at every time step. The calculation cost of the transformation is estimated at $\mathcal{O}(N_\theta^2 N_\phi \log N_\phi)$ owing to the absence of a fast algorithm for the Legendre transformation, which is as powerful as the fast Fourier transformation (FFT), where N_θ and N_ϕ are the maximum mode numbers in latitude and longitude, respectively. Thus, the computational cost of this method is significant and limits the achievable resolution. Owing to this, several numerical calculations of the geodynamo adopt the finite difference method to achieve high resolution (Kageyama et al., 2008; Miyagoshi et al., 2010). As explained above, when the near surface layer is included in the calculations, the typical convection scale decreases and a large num-

ber of grid points is required. The resolution is critical to assess the solar surface. Note that several studies using the finite difference method have been performed in the stellar or solar context using a moderate ratio for the speed of sound and convection velocity by adjusting the radiative flux and stratification (Käpylä et al., 2011, 2012). Although this type of approach offers insight for the maintenance of the mean flow and the magnetic field, proper reproduction using solar parameters, such as stratification, luminosity, ionization effect, and rotation, and direct comparison with observations cannot be achieved.

The reduced speed of sound technique (hereafter RSST, Rempel, 2005, 2006; Hotta et al., 2012b) can overcome such drawbacks while avoiding the severe time step caused by the speed of sound. In the RSST, the equation of continuity is replaced by

$$\frac{\partial \rho}{\partial t} = -\frac{1}{\xi^2} \nabla \cdot (\rho \mathbf{v}).$$

(1.19)

Then the speed of sound is reduced ξ times, but the dispersion relation for sound waves remains; the wave speed decreases equally for all wavelengths. This technique does not change the hyperbolic character of the equations, which can be integrated explicitly. Owing to this hyperbolicity, only local communication is required. This decreases the communication overhead in parallel computing. Simple algorithms and low-cost communication significantly facilitate high-resolution calculations. Hotta et al. (2012b) investigated the validity of the RSST in a thermal convection problem. They concluded that the RSST is valid when the Mach number, defined using the RMS (root mean square) velocity and the reduced speed of sound $\hat{c}_s$, is smaller than 0.7. Another advantage of this method is the accessibility to the real solar surface with inhomogeneous ξ. The Mach number substantially varies in the solar

convection zone. When moderate or no reduction in the speed of sound is used in the near surface layer while using a large ξ around the bottom part of the convection zone, the properties of the thermal convection, even including the surface, is properly investigated without losing the physics. It is confirmed in Hotta et al. (2012b) that the inhomogeneous ξ is valid when the Mach number is less than 0.7.

5   Thesis Goals

This thesis has three goals.

1. To develop the numerical code for effectively managing the huge number of CPUs ($\sim 10^5$) in a good performance with the reduced speed of sound technique in the spherical geometry. Even with the RSST, there are further requirements for treating the near surface layer in spherical geometry, such as the partial ionization effect of hydrogen and helium and the severe time step caused by the convergence of the grid spacing around the pole. The development of such complex numerical code with good scaling and performance requires sophisticated algorithms and detailed tuning for specific supercomputers. These steps are shown in Part II

2. To achieve the unprecedented resolution and small-scale convection with unprecedented higher upper boundary and attain significant scale gap in the thermal convection between the middle of the convection zone and the near surface layer. This will enable us to address how small-scale convection in the near surface layer influences the convection in the deeper layers. In addition, higher resolution makes the convection significantly turbulent, which allows to

better understand the generation and transport of small-scale magnetic field. These are discussed in Part III. Note that, in Part III, no rotation is taken into account to focus on the effects of turbulent convection.

3. To achieve the near surface shear layer with rotation. In this layer, the influence of the rotation is significantly different from that in the deeper convection zone. This means that the time and spatial scales of thermal convection change significantly. Although including these scales in the numerical calculations is difficult and challenging, the proposed high-performance method and numerical code can do it. This is discussed in Part IV.

In Part V, we summarize the thesis results and discuss the conclusion.

Part II
Basic Equations and Development of Numerical Code

本章については、5 年以内に雑誌等で刊行予定のため、非公開。

Part III
Structure of Convection and Magnetic Field without Rotation

本章については、5 年以内に雑誌等で刊行予定のため、非公開。

Part IV
Reproduction of Near Surface Shear Layer with Rotation

本章については、5 年以内に雑誌等で刊行予定のため、非公開。

Part V
Concluding Remarks

6 Summary of Thesis

The achievements and the important findings in this thesis are summarized in this part. In this thesis we focus on the interaction of the small-scale and large-scale

convection in the solar and stellar interior. Although this requires huge numerical resources and technical innovation, we succeed in simultaneously reproducing them. Then the achievements of this thesis provide significant understanding in the convection zone, such as the convection structure itself, the generation and transport of the magnetic field and the maintenance mechanism of the differential rotation.

6.1 Achievements

1. We significantly improve the ability of the numerical calculation of the solar and stellar global convection.

   Taking advantage of the reduced speed of sound technique as well as some other numerical techniques introduced in Part II, we develop the efficient numerical code for the solar global flow. The numerical code efficiently scales up to 10^5 cores and shows a good performance (14 % to the peak and 3×10^5 grid update/core/s). This is able to cover the broad spatial and temporal range of the plasma in the solar and stellar convection zone.

2. 10 Mm-scale convection is reproduced in the solar global convection for the first time.

   In the previous study, on account of lack of the resolution and large diffusivity, only the ~ 50 Mm-scale convection is achieved around their upper boundary (Miesch et al., 2008). Because we succeed in increasing the resolution and adopting the higher upper boundary, we can establish the 10 Mm-scale convection even in the global computation domain for the sun. This is reported in Part III.

3. The NSSL is reproduced for the first time.

The reproduction of the NSSL requires simultaneous establishment of the small- and large-scale convection. This means that reproduction requires a large number of time integration and the grid points. This challenging purpose is achieved in this thesis taking advantage of the good efficiency of our developed numerical code. This is reported in IV.

6.2 Findings

1. The small-scale convection generated near the surface layer influences the relatively shallower layer in the convection zone ($> 0.9R_\odot$). In the deeper layer ($< 0.9R_\odot$) the influence is negligible.

2. The magnetic field preferentially appears in the downflow, because strong magnetic field is likely generated there. This causes the downward Poynting flux in the convection zone. Around the base of the convection zone ($< 0.85R_\odot$), the magnetic energy is accumulated by the Poynting flux. The local dynamo even in the large scale is effective.

3. The NSSL is maintained by the Reynolds stress. The convective motion under the small influence of the rotation transports the angular momentum radially downward. This causes the poleward meridional flow with increasing the amplitude along the radius in the upper convection zone. This meridional flow again causes a positive correlation $\langle v_r' v_\theta' \rangle$ in the near surface layer, which then transports the latitudinal momentum radially upward. In the deeper convection zone, the correlation $\langle v_r' v_\theta' \rangle$ is negative owing to the Coriolis force, which transports the latitudinal momentum radially downward. The force by this momentum transport maintains the NSSL in our calculation. We argue that

this is a possible mechanism for the solar case.

7 Remaining problems and Future Work

7.1 Comparison with Helioseismology

Most recent observation by Hanasoge et al. (2012) using the local helioseismology technique estimates the internal structure of the thermal convection. Fig. 5.10 shows their result. They constraint the amplitude of the horizontal velocity associated with the solar convection for the modes with horizontal harmonics $\ell < 60$. The flow speed in this scale is substantially smaller than the result with the ASH code (by two orders of magnitude at maximum). The spectra in this thesis show similar amplitude to that of the ASH code results even with higher resolution and the higher upper boundary. In the current situation, both results of numerical simulation and helioseismology are under debate. A sophisticated comparison between them should be continued to understand the real structure of the solar global convection.

7.2 Proper Reproduction of Solar Differential Rotation

There is another problem still remaining for the differential rotation reported from the ASH code group (Featherstone and Miesch, 2013, in prep). They investigated the dependence of the differential rotation on the thermal diffusivity and the kinetic viscosity, which is believed to be very small in the real solar interior. They found that if the thermal diffusivity is small ($< 3 \times 10^{12}$ cm^2 s^{-1}), the polar region is accelerated, i.e. anti-solar differential rotation is obtained. When the thermal diffusivity is small, the entropy gradient near the surface becomes large and the generated thermal convection velocity becomes larger. This means the Rossby num-

インターネット公表に関する同意が
得られなかったため非公表

Figure 5.10: Figure from Hanasoge et al. (2012). Solid lines show the results by the local helioseismology. Blue and red lines are the results that correspond to horizontal velocities at $r = 0.92R_\odot$ and $r = 0.96R_\odot$, respectively. Dashed-dotted lines show the result calculated with the ASH code. Blue and red lines are the results that correspond to horizontal velocities at $r = 0.92R_\odot$ and $r = 0.979R_\odot$. l is the horizontal wavenumber.

ber becomes large. Because in the sun, the Rossby number is thought to be around unity, i.e., the effects of the Coriolis force and the convection are similar, the slight change in the convection velocity can cause significant change in the correlation terms ($\langle v_r' v_\phi' \rangle$ and $\langle v_\theta' v_\phi' \rangle$), the meridional flow and the differential rotation.

This problem might be caused by the limited resolution in the solar global convection simulations. The turbulence in the thermal convection is thought to have the power law distribution from the injection scale to the Kolmogorov dissipation scale. Although the unresolved scale convection can also transport the energy, we ignore them. As a consequence, our resolved scale must transport too much energy and must have too large an amplitude in the velocity. The improvement in this thesis for increasing the resolution will contribute to this fundamental issue in the future.

31

Part VI
Appendix

本章については、5 年以内に雑誌等で刊行予定のため、非公開。

References

Augustson, K., Rast, M., Trampedach, R., & Toomre, J. 2011, Journal of Physics Conference Series, 271, 012070

Basu, S., et al. 1997, MNRAS, 292, 243

Beck, J. G. 2000, Sol. Phys., 191, 47

Browning, M. K., Miesch, M. S., Brun, A. S., & Toomre, J. 2006, ApJ, 648, L157

Brun, A. S., Miesch, M. S., & Toomre, J. 2004, ApJ, 614, 1073

—. 2011, ApJ, 742, 79

Brun, A. S., & Toomre, J. 2002, ApJ, 570, 865

Busse, F. H. 1970, Journal of Fluid Mechanics, 44, 441

Charbonneau, P., Christensen-Dalsgaard, J., Henning, R., Larsen, R. M., Schou, J., Thompson, M. J., & Tomczyk, S. 1999, ApJ, 527, 445

Cheung, M. C. M., Moreno-Insertis, F., & Schüssler, M. 2006, A&A, 451, 303

Christensen-Dalsgaard, J. 2002, Reviews of Modern Physics, 74, 1073

Christensen-Dalsgaard, J., et al. 1996, Science, 272, 1286

Corbard, T., & Thompson, M. J. 2002, Sol. Phys., 205, 211

Duvall, Jr., T. L., Jefferies, S. M., Harvey, J. W., & Pomerantz, M. A. 1993, Nature, 362, 430

Ghizaru, M., Charbonneau, P., & Smolarkiewicz, P. K. 2010, ApJL, 715, L133

Giles, P. M., Duvall, T. L., Scherrer, P. H., & Bogart, R. S. 1997, Nature, 390, 52

Gilman, P. A., & Miller, J. 1981, ApJS, 46, 211

Glatzmaier, G. A. 1984, Journal of Computational Physics, 55, 461

Haber, D. A., Hindman, B. W., Toomre, J., Bogart, R. S., Larsen, R. M., & Hill, F. 2002, ApJ, 570, 855

Hanasoge, S. M., Duvall, T. L., & Sreenivasan, K. R. 2012, Proceedings of the National Academy of Science, 109, 11928

Hathaway, D. H. 1996, ApJ, 460, 1027

Hathaway, D. H., et al. 1996, Science, 272, 1306

Hotta, H., Rempel, M., & Yokoyama, T. 2012a, ApJL, 759, L24

Hotta, H., Rempel, M., Yokoyama, T., Iida, Y., & Fan, Y. 2012b, A&A, 539, A30

Hotta, H., & Yokoyama, T. 2011, ApJ, 740, 12

Howe, R. 2009, Living Reviews in Solar Physics, 6, 1

Kageyama, A., Miyagoshi, T., & Sato, T. 2008, Nature, 454, 1106

Käpylä, P. J., Mantere, M. J., & Brandenburg, A. 2012, ApJL, 755, L22

Käpylä, P. J., Mantere, M. J., Guerrero, G., Brandenburg, A., & Chatterjee, P. 2011, A&A, 531, A162

Kitchatinov, L. L., & Rüdiger, G. 1995, A&A, 299, 446

Küker, M., & Stix, M. 2001, A&A, 366, 668

Miesch, M. S. 2005, Living Reviews in Solar Physics, 2, 1

Miesch, M. S., Brun, A. S., De Rosa, M. L., & Toomre, J. 2008, ApJ, 673, 557

Miesch, M. S., Brun, A. S., & Toomre, J. 2006, ApJ, 641, 618

Miesch, M. S., Elliott, J. R., Toomre, J., Clune, T. L., Glatzmaier, G. A., & Gilman, P. A. 2000, ApJ, 532, 593

Miesch, M. S., & Hindman, B. W. 2011, ApJ, 743, 79

Miyagoshi, T., Kageyama, A., & Sato, T. 2010, Nature, 463, 793

Pietarila Graham, J., Cameron, R., & Schüssler, M. 2010, ApJ, 714, 1606

Rempel, M. 2005, ApJ, 622, 1320

—. 2006, ApJ, 647, 662

Rempel, M., & Schüssler, M. 2001, ApJL, 552, L171

Schou, J., et al. 1998, ApJ, 505, 390

Stix, M. 2004, The sun : an introduction, 2nd edn., Astronomy and astrophysics library, (Berlin: Springer), ISBN: 3-540-20741-4

Thompson, M. J., Christensen-Dalsgaard, J., Miesch, M. S., & Toomre, J. 2003, ARAA, 41, 599

Vögler, A., & Schüssler, M. 2007, A&A, 465, L43

Weber, M. A., Fan, Y., & Miesch, M. S. 2011, ApJ, 741, 11

Zhao, J., Bogart, R. S., Kosovichev, A. G., Duvall, Jr., T. L., & Hartlep, T. 2013, ApJL, 774, L29

Zwaan, C. 1987, ARAA, 25, 83